

The theory of kinks — I. A semi-analytic model of velocity perturbations due to planet-disc interaction

Francesco Bollati^{1*}, Giuseppe Lodato¹, Daniel J. Price² and Christophe Pinte^{2,3}

¹*Dipartimento di Fisica, Università degli Studi di Milano, Via Celoria 16, Milano, Italy*

²*School of Physics and Astronomy, Monash University, Clayton, Vic 3800, Australia*

³*Université Grenoble Alpes, CNRS, IPAG, F-38000 Grenoble, France*

Accepted XXX. Received YYY; in original form ZZZ

ABSTRACT

A new technique to detect protoplanets is by observing the kinematics of the surrounding gas. Gravitational perturbations from a planet produce peculiar ‘kinks’ in channel maps of different gas species. In this paper, we show that such kinks can be reproduced using semi-analytic models for the velocity perturbation induced by a planet. In doing so we i) confirm that the observed kinks are consistent with the planet-induced wake; ii) show how to quantify the planet mass from the kink amplitude; in particular, we show that the kink amplitude scales with the square root of the planet mass for channels far from the planet velocity, steepening to linear as the channels approach the planet; iii) show how to extend the theory to include the effect of damping, which may be needed in order to have localized kinks.

Key words: planet-disc interactions — planets and satellites: detection — protoplanetary discs — methods: analytical

1 INTRODUCTION

Observations of planet-forming and planet-hosting discs have been revolutionized by the high spatial and spectral resolution of the Atacama Large Millimetre/submillimetre Array (ALMA) at mm-wavelengths. Initial observations in the dust continuum revealed significant substructures in the form of rings (ALMA Partnership et al. 2015; Long et al. 2018; Andrews et al. 2018), spirals (Pérez et al. 2016; Huang et al. 2018), horseshoes (van der Marel et al. 2013) and warps (e.g. Kraus et al. 2020). A common —though not unique— explanation for these structures is the dynamical interaction with either a stellar or sub-stellar companion, or a planet embedded in the disc. Rings and gaps in particular can be explained by the interaction of a Jupiter-mass planet with the dusty disc (Dipierro et al. 2015, 2018; Veronesi et al. 2020). If planets are responsible for the creation of rings and gaps, the frequent occurrence rate of these substructures implies that massive planets may be already formed when the star is ≤ 1 Myr old, meaning that planet formation occurs while star formation is ongoing. Explaining how a population of giant planets at tens of au separation can be already in place at such a young age challenges current models of planet formation (e.g. Zhang et al. 2018; Lodato et al. 2019).

The above conclusion assumes that gaps and rings indicate planets — an indirect inference. A direct connection between a gap and one (or actually two) planets came with the observation of the PDS70 system (Keppler et al. 2018, 2019), where two directly imaged planets lie within a large dust gap.

More recently, line observations of gas species in the disc, such as the various CO isotopologues, have provided additional clues. Maps of the integrated line emission indicate that gas and dust distribution

is not the same, with the dust disc smaller than the gas disc (Ansdell et al. 2018; Facchini et al. 2019), presumably related to radial drift of mm-sized grains (but see Trapman et al. 2019). Line emission also allows one to probe the gas kinematics — both small scale turbulence (Flaherty et al. 2015, 2018, 2020) and large scale ordered motion, e.g. Keplerian rotation of the disc.

Deviations from Keplerian motion offer a novel and effective way to find embedded planets, whose gravitational pull locally perturbs the gas kinematics. Such kinematical signatures of planets have been observed in four different ways. First, through the analysis of the rotation curve as derived from CO emission (Teague et al. 2018), where a gap-opening planet reveals itself as a modification of the radial pressure profile, which in turn affect the rotation curve. Secondly, through the meridional circulation inside planetary gap, as laid out in Fung & Chiang (2016), Dong et al. (2019) and Teague et al. (2019). Thirdly, through the presence of a so-called ‘Doppler flip’ in the moment 1 map of the gas (Casassus & Pérez 2019). Finally, one may search for characteristic “kinks” in individual channel maps, which appear in a limited number of channels and are spatially located close to the planet position (Pinte et al. 2018, 2019, 2020). By comparing the ALMA data to hydrodynamical simulations, Pinte et al. (2018, 2019, 2020) were able to constrain the mass of the planets responsible for the kinks. However, a detailed fitting procedure is made difficult by the need for 3D hydrodynamical simulations and the computational expense of fully exploring the parameter space.

Goldreich & Tremaine (1979, 1980) and Papaloizou & Lin (1984) first developed the theory of the interaction between a gas disc and an embedded planet. The perturbing gravitational potential due to the planet excites density waves in the disc — launched at resonant locations, the Lindblad resonances — which propagate away from the planet, eventually becoming non-linear and steepening into shocks. Goodman & Rafikov (2001) and Rafikov (2002) (hereafter GR01;

* E-mail: fbollati@uninsubria.it

R02) analysed the linear and non-linear density waves produced by a planet, considering mainly the density perturbations created by the wake. In principle, such a theory can be used to compute the velocity perturbations, too, and thus provide the theory needed to interpret line observations of planet-hosting discs. This is our aim in the present paper.

This paper is organized as follows: Section 2 covers the basic theoretical framework of the model. In Section 3 we derive the velocity perturbations due to planet-disc interaction and the corresponding channel maps. In Section 4 we discuss our results, with our conclusions presented in Section 5.

2 THEORETICAL FRAMEWORK

2.1 The shape of the wake

As pointed out by Ogilvie & Lubow (2002), the linear theory of planet disc interaction developed by Goldreich & Tremaine (1979, 1980) does not provide information about the shape of the planet wake, since the disc response is determined separately for each Fourier mode of the planet potential. However, simulations for a terrestrial planet revealed the formation of a one-armed spiral wake (e.g. Artymowicz et al. 2000). Ogilvie & Lubow (2002) explained this pattern as the result of constructive interference between density waves launched at different Lindblad resonances. They found that the planetary wake, in a frame corotating with the planet, lies on the curve

$$\varphi_{\text{wake}}(r) = \varphi_p - \text{sgn}(r - r_p) \frac{2}{3\varepsilon} \left[\left(\frac{r}{r_p} \right)^{3/2} - \frac{3}{2} \ln \left(\frac{r}{r_p} \right) - 1 \right], \quad (1)$$

where (r_p, φ_p) is the location of the planet in the disc in polar coordinates and $\varepsilon \equiv h(r)/r = \text{const}$ is the disc aspect ratio. By dropping the assumption of constant ε , the expression (1) assumes the more general form

$$\varphi_{\text{wake}}(r) = \varphi_p + \text{sgn}(r - r_p) \int_{r_p}^r \frac{\Omega(r') - \Omega_p}{c_0(r')} dr', \quad (2)$$

where $\Omega(r)$ and Ω_p are the disc and planet angular velocities and $c_0(r)$ is the unperturbed disc sound speed. These quantities are related to the local disc thickness $h(r)$ by

$$h(r) = \frac{c_0(r)}{\Omega(r)}, \quad (3)$$

which holds for a thin disc in vertical hydrostatic equilibrium with a barotropic equation of state. In the case of a Keplerian power-law disc, where $\Omega(r) = (GM_\star/r^3)^{1/2}$ and $c(r) = c_p(r/r_p)^{-q}$ with $q > 0$, Eq. (2) reads (R02)

$$\varphi_{\text{wake}}(r) = \varphi_p + \text{sign}(r - r_p) \left(\frac{h_p}{r_p} \right)^{-1} \left[\frac{(r/r_p)^{q-1/2}}{q-1/2} - \frac{(r/r_p)^{q+1}}{q+1} - \frac{3}{(2q-1)(q+1)} \right]. \quad (4)$$

The shape of the wake in the vicinity of the planet is found by introducing local Cartesian coordinates $x = r - r_p$, $y = r_p(\varphi - \varphi_p)$, expanding Eq. (1) to the lowest non-vanishing order in $x/r_p \ll 1$ and using (3). The result, expressed in units of $(2/3)h_p$, reads

$$y'_{\text{wake}} = -\text{sgn}(x') \frac{1}{2} x'^2, \quad (5)$$

where $x' = 3x/2h_p$ and $y' = 3y/2h_p$

Moreover, Ogilvie & Lubow (2002) reported that the density perturbation of the wake has non-trivial internal structure, consisting of both a trough and a larger peak, as found from numerical simulations of planet-disc interaction.

2.2 Linear perturbations in the shearing sheet approximation

GR01 and R02 studied the internal structure of the density perturbation by solving the Euler and continuity equations of a disc with adiabatic equation of state semi-analytically. They split the computation of the density perturbation into two spatial regimes (where different approximations apply): a linear regime (GR01) close to the planet and a nonlinear regime (R02) further away from it.

In the linear regime the disc response is computed in the shearing sheet approximation, within a box of size $(8/3)h_p$ around the planet, where h_p is disc thickness in correspondence of the planet. The disc equations are written in local Cartesian coordinates x , y in a corotating system centered on the planet. In this frame the planet wake is steady, so that the time derivatives of the perturbations vanish. The fluid equations are i) linearized in the amplitude of small velocity and density perturbations and ii) the shearing sheet approximation is applied by assuming the homogeneity of the surface density Σ_0 and sound speed c_0 and by approximating the unperturbed disc motion to a linear shear flow. The planet disturbance enters the equations as a point-like gravitational perturbation at the origin. No other effects related to its presence are considered.

By writing the resulting equations in Fourier space (k_x, k_y) , GR01 obtained an ordinary differential equation for the Fourier components of the azimuthal velocity perturbation v , while the Fourier components of the radial velocity perturbation u and density perturbation $\sigma = \Sigma_1/\Sigma_0$ are given by algebraic relations (Equation 20 of GR01). For clarity, we report the basic equations here below:

$$\begin{aligned} \frac{d^2 \hat{v}}{d\tau^2} + \left[\kappa_p^2 + c_p^2 k^2(\tau) \right] \hat{v} &= -ik_y \frac{d\hat{\Phi}_p}{d\tau} + 2ik_x(\tau) B_p \hat{\Phi}_p, \\ \hat{u} &= -\frac{1}{c_p^2 k_y^2 + 4B_p^2} \left[2iB_p k_y \hat{\Phi}_p + 2B_p \frac{d\hat{v}}{d\tau} - c_p^2 k_x(\tau) k_y \hat{v} \right], \\ \hat{\sigma} &= \frac{i}{c_p^2 k_y^2 + 4B_p^2} \left[ik_y^2 \hat{\Phi}_p + k_y \frac{d\hat{v}}{d\tau} + \hat{v} k_x(\tau) 2B_p \right]. \end{aligned} \quad (6)$$

The Fourier transforms of the velocity and density perturbations $(\hat{v}, \hat{u}, \hat{\sigma})$ are functions of τ and k_y , where $\tau = -k_x/2A_p k_y$ and $A_p = (r\Omega')/2|_{r_p}$ is the first Oort constant at r_p . In Eqs. (6) we also see the second Oort constant $B_p = (A + \Omega)|_{r_p}$, the epicyclic frequency $\kappa_p = (4\Omega B)^{1/2}|_{r_p}$ and the local sound speed $c_p \equiv c_0(r_p)$ of the disc. The quantity $\hat{\Phi}_p$ in the r.h.s. of Eqs. (6) is the Fourier transform of the planet potential

$$\hat{\Phi}_p = -\frac{2\pi G M_p}{k}, \quad (7)$$

where M_p is the planet mass and $k = \sqrt{k_x^2 + k_y^2}$. GR01 solved equations (6) numerically and computed σ in real-space (x, y) using a Fast-Fourier-Transform (FFT) algorithm. Following their numerical recipe, we solved the system (6) and transformed back to real-space to get also u and v , as well as σ .

The computation is carried out with dimensionless quantities using $(2/3)h_p$ as length unit, c_p as the unit of velocity and $m_{\text{th}} = (2/3)h_p c_p^2/G$ (Eq. 19 of GR01) as the mass unit, which, thanks to (3) and assuming Keplerian rotation, turns out to be the thermal mass

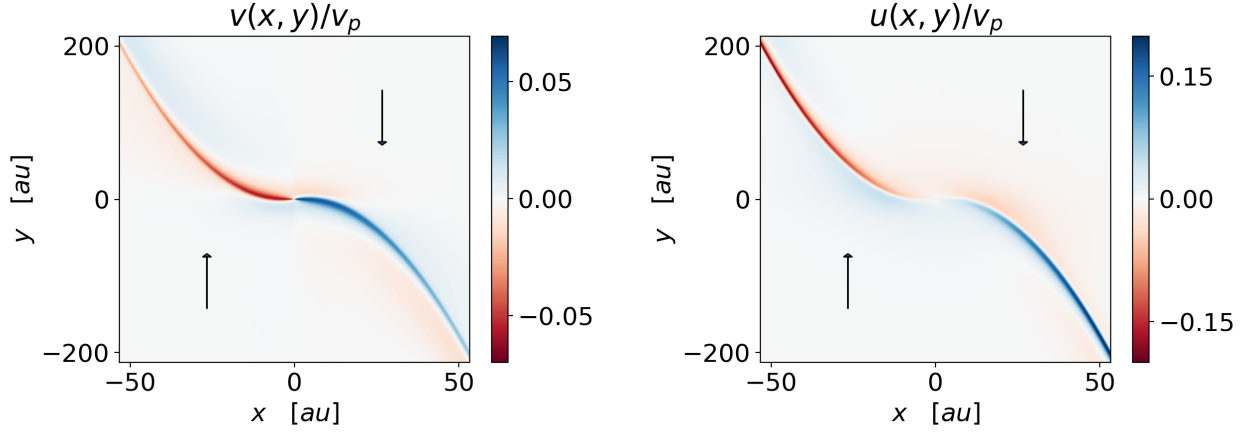


Figure 1. Linear azimuthal (left) and radial (right) velocity perturbations, in units of the planet Keplerian velocity v_p . Arrows show the direction of unperturbed disc flow in the local frame rotating with the planet.

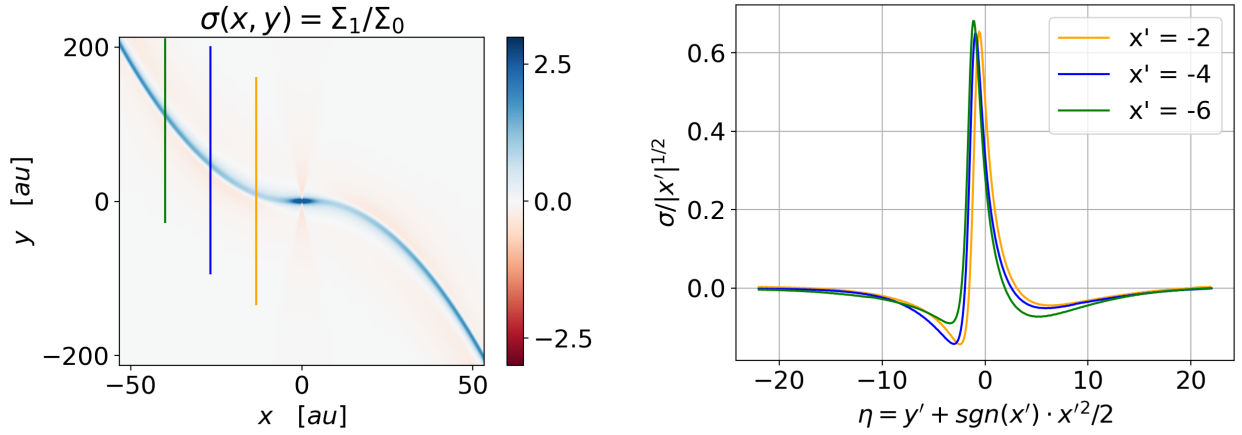


Figure 2. Left: Linear density perturbation in unit of local unperturbed disc surface density $\Sigma_0(r_p)$. Right: Surface density profiles for different radii inside the planetary orbit corresponding to the three vertical lines shown in the left panel (Cf. figure 1 of GR01). Primed coordinates are normalized with $(2/3)h_p$. The profile corresponding to $x' = -2$ is the initial condition of Eq. (10) for $r < r_p$, modulo a scaling factor, as discussed in section 2.3

$$m_{\text{th}} = \frac{2}{3} \left(\frac{h_p}{r_p} \right)^3 M_\star. \quad (8)$$

Definition (8) implies that the scale of the linear domain is that of the Hill radius $r_H = r_p(m_{\text{th}}/3M_\star)^{1/3}$. Using the units mentioned above and the fact that for Keplerian rotation $\Omega/2|A| = 2/3$ and $B/2|A| = 1/6$, the equation set (6) becomes

$$\begin{aligned} \frac{d^2 \hat{v}}{d\tau^2} + \left[k_y^2 (\tau^2 + 1) + \frac{4}{9} \right] \hat{v} &= -\text{sign}(k_y) \left(\frac{M_p}{m_{\text{th}}} \right) \frac{2\pi i}{3} \frac{\tau (\tau^2 + 4)}{(\tau^2 + 1)^{3/2}}, \\ \hat{u} &= -\frac{1}{k_y^2 + 1/9} \left[\frac{1}{3} \frac{d\hat{v}}{d\tau} - k_x(\tau) k_y \hat{v} - i \left(\frac{M_p}{m_{\text{th}}} \right) \frac{2\pi k_y}{3k} \right], \\ \hat{\sigma} &= \frac{i}{k_y^2 + 1/9} \left[k_y \frac{d\hat{v}}{d\tau} + \frac{1}{3} k_x(\tau) \hat{v} - i \left(\frac{M_p}{m_{\text{th}}} \right) \frac{2\pi k_y^2}{k} \right]. \end{aligned} \quad (9)$$

In order to solve these equations, we set the free parameter $M_p/m_{\text{th}} = 1$ and we considered a grid of $N_x \times N_y = 2^{12} \times 2^{13}$ points in (k_x, k_y) . Following GR01, we fixed the maximum $k_y = 8$ and for

each k_y in the grid we solved the first equation of (9) in the range $[-\tau_{\text{max}}, \tau_{\text{max}}]$ using $\tau_{\text{max}} = (N_y \pi / 8)^{1/2}$. As the initial condition we used $\hat{v} = d\hat{v}/d\tau = 0$ at $\tau = -\tau_{\text{max}}$. Having obtained $(\hat{v}, \hat{u}, \hat{\sigma})$, we multiplied these quantities by the pitch-angle filter, as described in GR01 §4, and finally transformed back to real-space via FFT algorithm. This computation provided us the velocity perturbations, in unit of c_p , and the density perturbation, in unit of the local surface density $\Sigma_p \equiv \Sigma_0(r_p)$, generated by a planet of mass m_{th} .

Figure 1 shows the resulting velocity perturbations for a planet with mass equal to the thermal mass located at $r_p = 100$ au embedded in a disc with $h_p/r_p = 0.1$, in orbit around a solar mass star ($M_\star = M_\odot$). With this choice of parameters, the planet mass is $m_{\text{th}} \approx 0.7 M_{\text{Jupiter}}$ and the linear box side measures $(8/3)h_p \approx 26.67$ au. The velocity perturbations are found to be anti-symmetric w.r.t the origin, as expected from the symmetries of Eqs. (9) and the properties of the Fourier transform, and lie on the curve (5), in agreement with Ogilvie & Lubow (2002).

Figure 2 illustrates the corresponding density perturbation, reproducing the result of GR01.

In this regime, all perturbations are linear in the planet mass, as it emerges from equations (9), therefore the perturbations for a generic planet mass M_p can be found with respect to a planet of mass m_{th} by rescaling the perturbations by a factor (M_p/m_{th}). Note that the linear approximation holds only for planet masses $\ll m_{\text{th}}$ that do not open a gap in the disc.

2.3 Global, non-linear evolution

We now turn to the structure of the density perturbation outside the linear domain, as first analysed by R02. We summarize here some relevant aspects. In R02, the density perturbation at the edges of the linear domain was used as the initial condition for the computation of the density perturbation away from the planet. In this regime, i) the shearing sheet approximation is abandoned, recovering the radial dependence of the disc structure, and ii) the disc equations are simplified via the tight-winding approximation. In addition, iii) the planet source term is dropped and iv) second order nonlinear terms are considered. Under these assumptions, R02 showed that the structure of the density perturbation, in a polar coordinate frame corotating with the planet¹, obeys the inviscid Burgers' equation²

$$\partial_t \chi + \text{sgn}(r - r_p) \chi \partial_\eta \chi = 0, \quad (10)$$

where χ is related to the density perturbation $\Sigma - \Sigma_0$ via

$$\chi \equiv \frac{\gamma + 1}{2} \frac{\Sigma - \Sigma_0}{\Sigma_0} g(r), \quad (11)$$

$$g(r) \equiv \frac{2^{1/4}}{r_p c_p \Sigma_p^{1/2}} \left(\frac{r \Sigma_0 c_0^3}{|\Omega - \Omega_p|} \right)^{1/2}, \quad (12)$$

γ is the disc adiabatic index and subscript 'p' denotes unperturbed quantities evaluated at r_p . The coordinates t and η in Equation (10) are spatial coordinates defined by

$$t(r) \equiv -\frac{r_p}{2h_p/3} \int_{r_p}^r \frac{\Omega(r') - \Omega_p}{c_0(r') g(r')} dr', \quad (13)$$

$$\eta(r, \varphi) \equiv \frac{r_p}{2h_p/3} [\varphi - \varphi_{\text{wake}}(r)], \quad (14)$$

where φ_{wake} is given by (2). Eqs. (13) and (14) can be thought of, respectively, as a coordinate along the spiral wake and as an azimuthal coordinate centered in the wake at the same radius. Hence, Eq. (10) describes the "evolution" of the azimuthal profile of the density perturbation along the spiral wake. For the case of a Keplerian power-law disc ($\Sigma_0(r) = \Sigma_p (r/r_p)^{-\delta}$, Eq. 4 and preceding text), the expression for $g(r)$ (Eq. 12) becomes

$$g(r) = 2^{1/4} \left(\frac{h_p}{r_p} \right)^{1/2} \frac{(r/r_p)^{5/4 - (\delta + 3q)/2}}{|1 - (r/r_p)^{3/2}|^{1/2}}, \quad (15)$$

giving the integral for $t(r)$ (Eq. 13) in the form

$$t(r) = \frac{-3}{2^{5/4} (h_p/r_p)^{5/2}} \int_1^{r/r_p} (1 - x^{3/2}) |1 - x^{3/2}|^{1/2} x^w dx, \quad (16)$$

¹ In this frame the perturbation is stationary, as in the linear regime.

² In R02's equation for χ , the $\text{sgn}(r - r_p)$ is replaced by a minus sign since only the case $r < r_p$ is considered. The symmetry of σ suggests that in the general case a $\text{sgn}(r - r_p)$ term must be present, as confirmed by following R02's derivation of the equation for χ (Appendix A of R02) in the case $r > r_p$.

where $w \equiv -11/4 + (\delta + 5q)/2$ and we substituted $x \equiv r/r_p$. Since t is always positive one may also simplify further to

$$t(r) = \left| \frac{-3}{2^{5/4} (h_p/r_p)^{5/2}} \int_1^{r/r_p} |1 - x^{3/2}|^{3/2} x^w dx \right|, \quad (17)$$

which is the integral we solve in the code.

In order to solve Eq. (10), we need to specify the initial condition. We observe that Eq. (10) consists of two equations, one for $r > r_p$ and the other for $r < r_p$, hence two initial profiles, $\chi_+(\eta)$ and $\chi_-(\eta)$, are required. These functions are found by taking the limit of χ in the linear regime and by evaluating the result at the edges $r_\pm = r_p \pm (4/3)h_p$ of the linear box domain. More precisely, in linear and shearing sheet approximation, χ reduces to (cf. Eq. 35 of R02)

$$\chi(t, \eta) \approx \frac{\gamma + 1}{2^{3/4}} \frac{M_p}{m_{\text{th}}} \frac{\sigma(x', \eta - x'^2 \text{sgn}(x')/2)}{\sqrt{x'}} \quad (18)$$

where $\sigma = (\Sigma - \Sigma_0)/\Sigma_0$ is the density perturbation³ computed in the linear regime for the thermal mass m_{th} , the factor M_p/m_{th} is due to the linear scaling of σ with M_p and the second argument of σ , y' , has been written using $\eta \simeq y' - y'_{\text{wake}}$, which is the form that Equation (14) assumes near the planet.

Figure 2 (right panel) shows the corresponding profiles of (18) for some example values of x' , modulo the prefactor $(M_p/m_{\text{th}})(\gamma + 1)2^{-3/4}$, for the case $r < r_p$. Since σ is symmetric with respect to the origin, the profiles of (18) for $r > r_p$ are simply flipped with respect to the y axis compared to those shown in Figure 2 (right panel). Then, the initial conditions χ_\pm of the problem (10) are given by (18) evaluated at $x' = (r_\pm - r_p)/(2h_p/3) = \pm 2$, the outer and inner boundaries of the linear domain. This corresponds to set the initial "time" of nonlinear "evolution" at $t_0 \simeq 1.89$.

Having computed the initial conditions for χ , we proceed to discuss its evolution under Equation (10).

From the theory of Burgers' equation (Whitham 1974) we know that each wave element of an initial profile travels with a characteristic speed that depends on the value of χ carried by that the wave element. More formally, a certain value χ is kept constant along the characteristic curve $(t, \eta(t))$ of speed $(\partial \eta / \partial t)_\chi = \text{sgn}(r - r_p) \chi$, since on such curve $d\chi/dt = 0$, as follows from Equation (10). In particular, high- χ elements move faster than low- χ ones and, as a consequence, the wave profile is distorted and eventually shocks (see Figure 3). As shown in Whitham (1974) Ch. 2.8, if the initial wave-form changes sign and has a finite range (as the profiles in Figure 2 do), an "N-wave" shape eventually develops, with two shocks of opposite signs moving in opposite directions. The areas of the two lobes of the N-wave are constant in time, since the flux across the point $\chi = 0$ that separates the lobes vanishes and the "mass" $\int_{\text{annulus}} \chi d\eta$ is conserved. In our case, the lobe areas are equal to each other because the conserved "mass" is zero⁴. Due to their time independence, the areas of the lobes can be found from the profile at t_0 . In our problem for $r < r_p$, such areas are given by

$$A \equiv \left| \int_{\tilde{\eta}}^{\infty} \chi_-(\eta) d\eta \right|, \quad (19)$$

³ We use the same symbol σ for both the density perturbation as a function of x, y and as a function of dimensionless x', y' , where it is implicit that $\sigma(x, y) = \sigma(x', y')$.

⁴ This is true because for every $t \geq t_0$, that is for every radius both $r \geq r_+$ and $r \leq r_-$, the integral of χ on the whole range of η , a disc annulus, must vanish $\int \chi d\eta \propto \int_0^{2\pi} (\Sigma - \Sigma_0) d\varphi = 0$, since the wake density perturbation alters the azimuthal density profile of the annulus but not its mass.

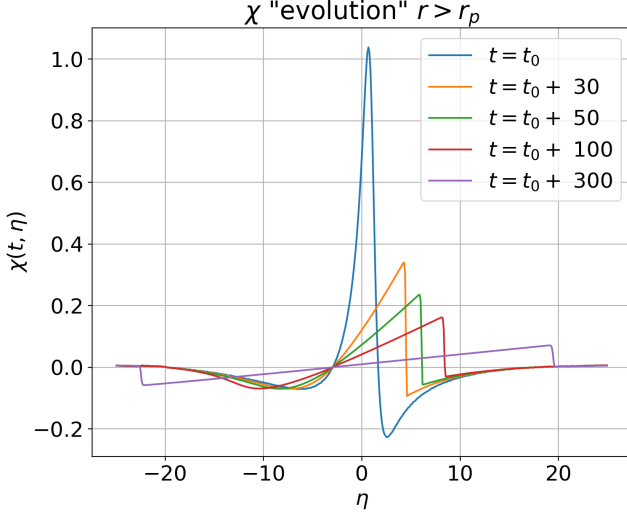


Figure 3. Time evolution of the numerical solution χ of Eq. (10) for $r > r_p$ in case of $M_p = m_{\text{th}}$. The wave elements move to the right at speed $(\partial\eta/\partial t)_\chi = \chi$. In this way the initial negative hump at $\eta < 0$ moves to the left and shocks, preserving the initial area of the hump. On the other hand, the negative hump at $\eta > 0$, is absorbed into the shock moving to the right formed by the positive peak, whose area is reduced by that of the incorporated negative hump. Asymptotically χ develops an N-wave profile.

where $\tilde{\eta} \approx 2.96$ is the point $\chi_-(\tilde{\eta}) = 0$ separating the lobes (see Fig. 2). It turns out that the lobes areas for $r > r_p$ are given by (19) as well because of the symmetry of σ .

Concerning the dependence on the planet mass, we know that the height and width of the lobes scale as $A^{1/2}(t - t_0)^{-1/2}$ and $A^{1/2}(t - t_0)^{1/2}$ (Whitham 1974), hence these quantities are both proportional to $M_p^{1/2}$, as it follows from (19) and $\chi_- \propto \sigma \propto M_p$.

The asymptotic N-wave solutions of (10) can be written in a form which comprises the two cases $r \lesseqgtr r_p$. This formula reads:

$$\chi(t, \eta) = \begin{cases} [\text{sgn}(r - r_p)\eta + \tilde{\eta}] / (t - t_0) & \eta \in [\eta_-, \eta_+] \\ 0 & \text{elsewhere} \end{cases} \quad (20)$$

where

$$\eta_{\pm} = -\text{sgn}(r - r_p)\tilde{\eta} \pm \sqrt{2A(t - t_0)}. \quad (21)$$

This solution of Equation (10) applies asymptotically, i.e. far away from the planet. In order to compute the density perturbation near the planet we need to find a numerical solution of Equation (10). We solved Equation (10) using a Godunov scheme on a grid of $N_\eta \times N_t = 509 \times 14966$ points.

Figure 3 shows the time evolution of the solution (recalling that ‘time’ here is a coordinate related to distance along the wake) for the case $r > r_p$. The solution for $r < r_p$ can be found noting that if χ_{out} is the solution of (10) for $r > r_p$, then $\chi_{\text{in}}(t, \eta) \equiv \chi_{\text{out}}(t, -\eta)$ satisfies (10) for $r < r_p$. From Figure 3, in which $M_p = m_{\text{th}}$, we see that after a time $\approx t_\infty \equiv t_0 + 300$, the profile displays a N-wave shape and therefore it can be described with the asymptotic N-wave solution (20). For a generic planet mass, the time t_∞ after which the profile is well approximated by the N-wave is $t_\infty = t_0 + 300(m_{\text{th}}/M_p)$, according to Eq. (39) in R02.

3 VELOCITY PERTURBATIONS AND CHANNEL MAPS

While the spiral density perturbation resulting from planet-disc interaction is well understood, the associated velocity perturbations have not received the same attention. But this is needed in order to interpret the kinematical signatures of embedded planets!

3.1 Velocity perturbations in nonlinear regime

To produce the kinks seen in the channel maps, we first need to compute the disc velocity field in the presence of a planet. We already achieved this in the vicinity of the planet in section 2.2. Here we complete the calculation by computing the nonlinear velocity perturbations, providing their relation to the density perturbation χ . In doing so, we rely on the work of R02, keeping the same notation.

As shown in section 2.2 of R02, the nonlinear radial velocity perturbation is⁵

$$u = -\text{sgn}(r - r_p) \frac{2(c_0 - c)}{\gamma - 1}. \quad (22)$$

This equation can be rewritten in terms of the quantity $\psi = (c - c_0)(\gamma + 1)/[c_0(\gamma - 1)] \ll 1$ (Equation A2 of R02) to yield

$$u = \text{sgn}(r - r_p) \frac{2c_0}{\gamma + 1} \psi. \quad (23)$$

On the other hand, the azimuthal velocity perturbation, expressed as a function of ψ , reads (see Equation A8 of R02)

$$v \approx -2 \frac{c_0^2}{\Delta\Omega r} \frac{1}{\gamma + 1} \psi. \quad (24)$$

where $\Delta\Omega \equiv \Omega - \Omega_p$. Now we write u and v in terms of χ using the relation

$$\chi = g\psi + \mathcal{O}(\psi^2), \quad (25)$$

which follows from Equation (A3) of R02 and definition (11). By replacing (25) in (23) and (24), discarding $\mathcal{O}(\psi^2)$ terms⁶ and using Equation (12), we obtain the nonlinear velocity perturbations

$$u(r, \varphi) = \text{sgn}(r - r_p) \Lambda_p f_u(r) \chi(t, \eta), \quad (26)$$

$$v(r, \varphi) = \text{sgn}(r - r_p) \Lambda_p f_v(r) \chi(t, \eta), \quad (27)$$

where

$$\Lambda_p = \frac{2^{3/4}}{\gamma + 1} r_p c_p \Sigma_p^{1/2}, \quad (28)$$

$$f_u(r) = \left[\frac{|\Delta\Omega(r)|}{r \Sigma_0(r) c_0(r)} \right]^{1/2}, \quad (29)$$

$$f_v(r) = \left[\frac{c_0(r)}{|\Delta\Omega(r)| \Sigma_0(r) r^3} \right]^{1/2}, \quad (30)$$

and $\chi = \chi(t(r), \eta(r, \varphi); M_p)$ is the solution to Equation (10). The term (30) formally diverges at $r = r_p$ but we need not worry since equations (26)–(30) hold in the nonlinear regime, outside the linear box centered in r_p where the singularity occurs. If the disc is a power-law Keplerian disc, with surface density and sound speed profiles

⁵ Actually R02 presents u without the coefficient $-\text{sgn}(r - r_p)$, since he considers only the case $r < r_p$. By following R02’s derivation of u (section 2.2 of R02) for $r > r_p$ we easily obtain Equation (22).

⁶ As in R02’s derivation of Eq. (10), where nonlinear terms proportional to $\psi\partial_t\psi$ are retained while ψ^2 terms are discarded, since the tidal perturbation is assumed to be weak and tightly wound.

$\Sigma_0(r) = \Sigma_p(r/r_p)^{-\delta}$ and $c_0(r) = c_p(r/r_p)^{-q}$, the terms $\Lambda_p f_u(r)$ and $\Lambda_p f_v(r)$ read

$$\Lambda_p f_u(r) = c_p \left(\frac{h_p}{r_p} \right)^{-1/2} \frac{2^{3/4}}{\gamma+1} \left(\frac{r}{r_p} \right)^{(\delta+q-1)/2} \left| \left(\frac{r}{r_p} \right)^{-3/2} - 1 \right|^{1/2}, \quad (31)$$

$$\Lambda_p f_v(r) = c_p \left(\frac{h_p}{r_p} \right)^{1/2} \frac{2^{3/4}}{\gamma+1} \left(\frac{r}{r_p} \right)^{(\delta-q-3)/2} \left| \left(\frac{r}{r_p} \right)^{-3/2} - 1 \right|^{-1/2}, \quad (32)$$

where we also used Equation (3).

From Equations (26)–(30) it follows that the azimuthal profiles of u and v have the same shape of χ — rescaled by the factors $\Lambda_p f_u(r)$ and $\Lambda_p f_v(r)$. Therefore, asymptotically, they display a N-wave shape with the same scaling properties $\propto M_p^{1/2}$ of χ , as discussed in section 2.3.

The velocity perturbations (26)–(30) in addition to those computed in the linear regime (section 2.2) represent the velocity disturbance caused by the planet wake. We assume that this is the planet-induced velocity substructure responsible for the observed kinks, although other origins have been suggested (e.g. Perez et al. 2015). Under this assumption, in the following sections we attempt to produce analytical kinks from the velocity perturbations of the wake and compare them to the observations.

3.2 Channel maps in a Keplerian disc

Before delving into the kinks, let us consider the line emission expected in a channel map in the absence of a planet, i.e. when the disc velocity field is unperturbed. We assume Cartesian coordinates such that the origin coincides with the star, the disc lies in the xy -plane and the z axis forms an angle θ with the line-of-sight \hat{n} (pointing towards the observer). In addition, the x, y axes are oriented such that $\hat{n} = (-\sin \theta, 0, \cos \theta)$, which corresponds to a disc with PA = 90° and inclination $i = \theta$.

If the disc motion is undisturbed and inviscid, the only non-vanishing component of the disc velocity field is the azimuthal component. Moreover, if we neglect terms of order $O((h/r)^2)$, this component can be approximated with the Keplerian velocity $v_K = (GM_\star/r)^{1/2}$. In this case we write the unperturbed disc velocity field as⁷

$$\mathbf{v}_0 = v_K(r) \mathbf{e}_\varphi = v_K(r) (-\sin \varphi, \cos \varphi, 0)^T. \quad (33)$$

Molecular-line observations probe the line-of-sight component of the gas which, for a Keplerian disc, assumes the form⁸:

$$v_{n,0} = \mathbf{v}_0 \cdot \hat{n} = v_K(r) \sin \theta \sin \varphi. \quad (34)$$

For a generic velocity field \mathbf{v} , the function $v_n(r, \varphi) = \mathbf{v}(r, \varphi) \cdot \hat{n}$ allow us to produce the corresponding channel maps. If the disc elements have a certain velocity field with non-zero component towards the observer ($v_n \neq 0$), then the emission will be Doppler-shifted. In a given channel map the emission is distributed along the regions of the

⁷ In this notation the disc flows in counterclockwise direction as seen from z . A disc in clockwise rotation w.r.t. the observer corresponds to an inclination angle $\theta \in [\pi/2, 3\pi/2]$.

⁸ Here we assume that the disc is 2D, hence a given line of sight only penetrates the disc at a given (r, φ) . In reality if we consider a 3D structure, a given line of sight goes through multiple regions in the disc with different (r, φ) , implying a velocity projection different from Eq. (34).

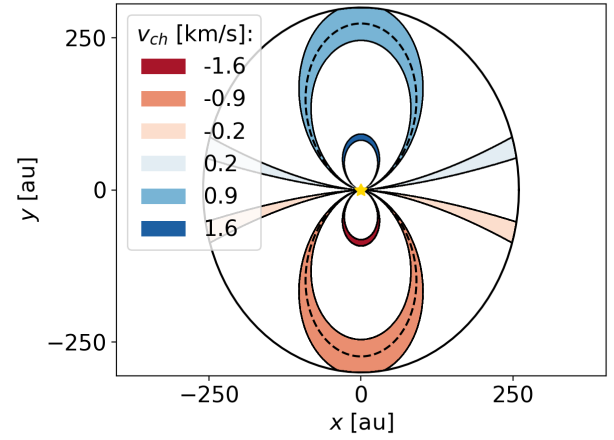


Figure 4. Channel maps for a Keplerian disc with inclination angle $\theta = \pi/6$ and velocity resolution $\Delta v = 0.05$ km/s. The dashed lines are examples of channel maps plotted from Eq. (36).

source that undergo the same Doppler-shift, i.e. the regions where v_n is equal to the channel velocity v_{ch} . Then, the disc elements (r, φ) of a channel map, or isovelocity curve, with channel velocity v_{ch} must satisfy the condition

$$v_n(r, \varphi) = v_{ch}. \quad (35)$$

If the disc is Keplerian, v_n is given by (34) and Equation (35) admits the solution

$$\tilde{r}(\tilde{\varphi}) = \frac{GM_\star}{v_{ch}^2} \left| \frac{\cos \theta}{\cos \tilde{\varphi}} \right| \frac{(\sin \theta \cos \theta \tan \tilde{\varphi})^2}{[1 + (\tan \tilde{\varphi} \cos \theta)^2]^{3/2}} \mathcal{H}(\sin \tilde{\varphi} \sin \theta v_{ch}), \quad (36)$$

where \mathcal{H} is the Heaviside step function and $\tilde{r}, \tilde{\varphi}$ are the polar coordinates in the plane perpendicular to the line-of-sight (the sky plane), with y -axis coinciding with the disc inclination axis (see Figure 4). Actually, in real measurements we always have a finite channel resolution Δv (which is typically of the order of 0.05 km/s), therefore the channel maps will be given by the set of disc elements such that

$$v_n(r, \varphi) \in [v_{ch} - \Delta v, v_{ch} + \Delta v]. \quad (37)$$

Figure 4 illustrates some examples of channel maps for a disc with a radius of 300 au in Keplerian rotation around a solar mass star (similar to Pinte et al. 2019), considering different channel velocities and an inclination angle $\theta = \pi/6$. In this Figure the channel maps have been created by “painting” the grid points of the disc⁹ that satisfy the condition (37). The patterns shown in Fig. 4 are known as *butterfly patterns* and are characteristic of discs in Keplerian rotation (e.g. Horne & Marsh 1986). In principle, a disturbance in the disc velocity field could be detected as a deviation from the butterfly pattern in the channel maps. The channel maps which are coloured in tones of red represent red-shifted molecular lines, while the channel maps in tones of blue are associated with blue-shifted emissions. The red-blue shift patterns are reversed if $\theta \in [\pi, 2\pi]$.

Having become familiar with the unperturbed shape of the isovelocity curves, we are now ready to add planets. To do so, in the

⁹ In this and other Figures, we discretised the disc using a Cartesian grid of $10^3 \times 10^3$ points.

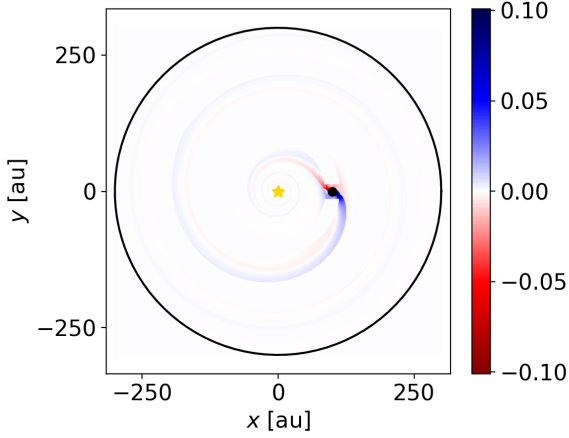


Figure 5. The velocity perturbation in the whole disc is non-vanishing along the spiral density wake. The black circle denotes the planet location.

following section we apply the planet velocity perturbations to the unperturbed Keplerian velocity field.

3.3 Analytic kinks

We use the linear and nonlinear velocity perturbations, computed respectively in section 2.2 and section 3.1, in order to predict the shape of the kinks arising from the planetary wake. In the presence of a planet, the velocity field at each point of the disc is given by the unperturbed Keplerian velocity (33) plus the radial and azimuthal velocity perturbations u and v :

$$\begin{aligned} \mathbf{v}(r, \varphi) &= (v_K(r) + v(r, \varphi))\mathbf{e}_\varphi + u(r, \varphi)\mathbf{e}_r \\ &= (u \cos \varphi - (v + v_K) \sin \varphi)\mathbf{e}_x + (u \sin \varphi + (v + v_K) \cos \varphi)\mathbf{e}_y. \end{aligned} \quad (38)$$

The application of these perturbations is split into linear and nonlinear regimes. In the linear regime for u and v we used the dimensionless velocity perturbations computed in section 2.2, rescaled by a factor $c_p(M_p/m_{\text{th}})$. These perturbations were applied to the disc grid points inside the linear box domain around the planet. In the nonlinear regime u and v were computed using equations (26) and (27), where the terms $\Lambda_p f_u$ and $\Lambda_p f_v$ are given by (31) and (32), choosing $\delta = 1$ and $q = 1/4$. For the term χ we used the numerical solution of Eq. (10) if $t < t_\infty$ and the analytical N-wave solution (20) for larger t .

In order to visualize how the disc velocity field is altered by the presence of the planet, we considered the quantity $\delta v \equiv (|\mathbf{v}| - |\mathbf{v}_0|)/|\mathbf{v}_0|$ where \mathbf{v} and \mathbf{v}_0 are the disc velocity in the presence and in the absence of the planet (Eqs. 38 and 33 respectively). Figure 5 shows the contour plot of δv for a system with $M_\star = M_\odot$, $R_{\text{disc}} = 300$ au, $\gamma = 5/3$ and $h_p/r_p = c_p/v_K(r_p) = 0.1$, which implies a thermal mass (8) of $m_{\text{th}} = 0.7M_{\text{Jupiter}}$. The planet has a mass $M_p = M_{\text{Jupiter}}$ and is located at $(r_p = 100$ au, $\varphi_p = 0)$. From this Figure we observe that the velocity perturbation along the planetary wake undergoes an abrupt sign reversal across the planet. This feature of the wake was suggested by Casassus & Pérez (2019) to infer the presence and location of a planet in the system HD 100546 through the corresponding ‘‘Doppler flip’’ in the first moment map.

The kinks in the channel maps arise due to the variation of the component along \hat{n} of the disc velocity that occurs in presence of a

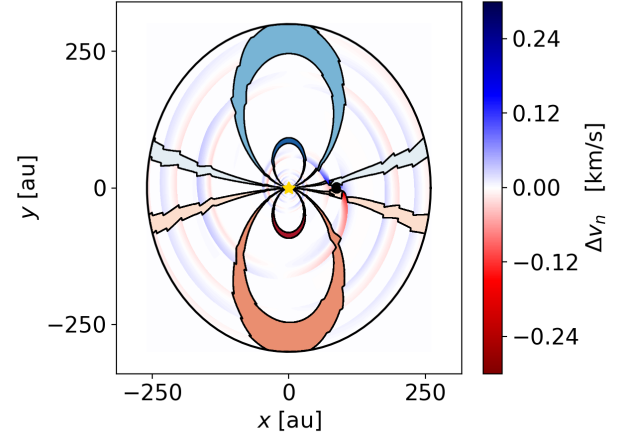


Figure 6. Analytical channel maps of Fig. 4 for a disc hosting a planet, with $\theta = \pi/6$ and channel velocity resolution $\Delta v = 0.05$ km/s. In the figure is also shown the contour of Δv_n (Eq. 40). The kinks appear in the whole disc almost every time a channel map crosses the spiral planetary wake.

planet. For an unperturbed disc, the gas velocity projected on \hat{n} is given by (34). Instead, if the disc hosts a planet, the dot product of Equation (38) and \hat{n} yields

$$v_n(r, \varphi) = \sin \theta [(v_K(r) + v(r, \varphi)) \sin \varphi - u(r, \varphi) \cos \varphi]. \quad (39)$$

As in the unperturbed case (see section 3.2), the analytical channel map with channel velocity v_{ch} is produced by ‘‘painting’’ the grid points such that $v_n(r, \varphi) \in [v_{\text{ch}} - \Delta v, v_{\text{ch}} + \Delta v]$.

Figure 6 shows the resulting channel maps. In the background of this figure we also show the quantity

$$\Delta v_n \equiv v_n - v_{n,0} = \sin \theta [v(r, \varphi) \sin \varphi - u(r, \varphi) \cos \varphi], \quad (40)$$

We observe that the velocity perturbations, once added to a Keplerian velocity field, give rise to the observed kinks. These are created when the planet wake crosses a velocity channel.

3.4 Velocity damping

Figure 6 shows that the theoretical kinks are present even in those channel maps that cross the wake in regions of the disc far away from the planet. This is in conflict with the observational and numerical evidence showing that kinks are localized near the planet (Pinte et al. 2018, 2019). While this may just be due to the finite beam resolution that would smear out the smaller kinks far from the planet, we also discuss here the hypothesis that this excess of kinks is due to a lack of damping of the analytical velocity perturbations as the wake travels away from the planet. Viscosity is known to damp density and velocity perturbations as they propagate across the disc (Shu 1984) and we thus apply an exponential damping to the velocity perturbations in order to recover the local behavior in the theoretical kinks.

Shu (1984) showed that a linear density wave excited at the m -th Lindblad resonance r_r undergoes viscous damping by a factor

$$\exp\left(-\int_{r_r}^r k_I dr'\right), \quad (41)$$

where

$$k_I = -\epsilon \frac{(7v_s/3)\kappa k_R^2}{2\pi G \Sigma_0 - 2c_0^2 |k_R|}, \quad (42)$$

where ν_s is the shear viscosity, $\epsilon = \pm 1$ at inner/outer Lindblad resonances and κ is the epicyclic frequency. The real part of the wave number k_R satisfies the Lin & Shu (1964) dispersion relation for tightly wound density waves in a two-dimensional gaseous disc, namely

$$m^2(\Omega - \Omega_p)^2 = \kappa^2 - 2\pi G \Sigma_0 |k_R| + c_0^2 k_R^2. \quad (43)$$

Equation (42) can be simplified with the following approximations. In the non-self gravitating limit we can neglect the term $2\pi G \Sigma_0$ in both equations (42) and (43). In addition, if we take the Lindblad resonance index $m \gg 1$ and we use $\kappa = \Omega$ (as in Keplerian rotation), Eq. (43) yields

$$|k_R| = m \frac{|\Delta\Omega|}{c}. \quad (44)$$

By replacing (44) in (42), assuming $\nu_s = \alpha hc$ (Shakura & Sunyaev 1973) and using (3), we obtain

$$k_I \approx -\epsilon \alpha m \frac{7|\Delta\Omega|}{6c_0}. \quad (45)$$

Under these approximations the damping factor (41) for the velocity perturbations launched at the m -th Lindblad resonance can be written as

$$\exp\left(\epsilon m \alpha \frac{7}{6} \int_{r_r}^r \frac{|\Delta\Omega|}{c_0} dr'\right). \quad (46)$$

The radial and azimuthal velocity perturbations u and v (Eqs. 26 and 27 in the nonlinear regime and those computed in section 2.2 for the linear regime) are the velocity perturbations associated with the planetary wake, which is the result of the constructive interference of the waves launched at several Lindblad resonances (section 2.1). Each of the waves excited at Lindblad resonances has a different viscous damping factor due to the dependence of (46) on the index m . Despite the fact that the perturbations u and v come from the superposition of waves with different damping factors, we introduce the disc viscosity in the model developed so far by applying to u and v a single exponential factor

$$\mathcal{D} = \exp\left(-\frac{7\alpha m}{6h_p} \left| \int_{r_p}^r |(r'/r_p)^{-3/2} - 1|(r'/r_p)^q dr' \right| \right), \quad (47)$$

which is obtained from Eq. (46) using $c_0 = c_p(r/r_p)^{-q}$, $\Omega = (GM_\star/r^3)^{1/2}$, Eq. (3) and $r_r \approx r_p$ (being $m \gg 1$). Then, the velocity perturbations in the presence of viscous damping, u_d and v_d , read

$$\begin{aligned} u_d(r, \varphi) &= \mathcal{D}(r)u(r, \varphi), \\ v_d(r, \varphi) &= \mathcal{D}(r)v(r, \varphi). \end{aligned} \quad (48)$$

In our treatment the coefficient (47) appears as a term that mimics the effect of viscosity, whose strength can be tuned by varying the parameter αm .

Figure 7 shows how the analytical kinks in the channel maps of Figure 6 are modified in presence of viscous damping. In order to evaluate (47) we assumed a sound speed profile index $q = 1/4$ and we tuned αm such that the kinks were sufficiently damped after about a half-winding of the wake, as it occurs in observations and numerical simulations. This led us to set $\alpha m = 0.5$.

We now use our analytic model for the channel maps to make a comparison with the channel map of the disc surrounding HD 163296 studied in Pinte et al. (2018). Figure 8 shows that the basic morphology of the kink is the same as in the observation reported in Pinte et al. (2018) when compared to the corresponding theoretical channel map created using the system parameters as derived by Pinte

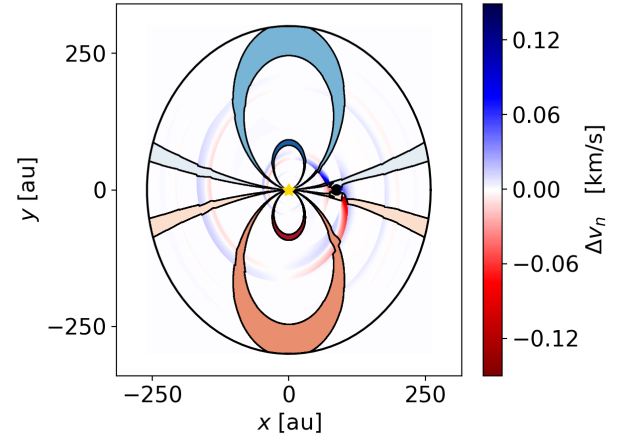


Figure 7. Analytical channel maps of Fig. 4 for a disc hosting a planet, with $\theta = \pi/6$ and channel velocity resolution $\Delta v = 0.05$ km/s. In the figure is also shown the contour of Δv_n (Eq. 40). The kinks appear only in the vicinity of the planet due to a viscous damping with $\alpha m = 0.2$.

et al. (2018), based on a comparison with their hydrodynamical simulations: a planet mass $M_p = 2M_{\text{Jupiter}}$ in orbit at $r_p = 270$ AU around a $1.9M_\odot$ star in a disc with inclination $i = 45^\circ$, PA = 33.75° , aspect ratio $h_p/r_p = 0.1$, power-law profiles $\Sigma_0 = \Sigma_p(r/r_p)^{-1}$, $c_0 = c_p(r/r_p)^{-1/4}$ and adiabatic index $\gamma = 5/3$.

Here we provided a model for the wave damping due to viscosity, but other mechanisms, whose discussion is beyond the aim of this paper, can play a significant role in mitigating the planet induced perturbations, such as the presence of a finite cooling timescale (Miranda & Rafikov 2020).

3.5 Dependence of the kink amplitude on the system parameters

Ultimately, we wish to understand how the kink amplitude can be used to measure the planet mass. For this we need to measure and interpret the “distance” of an isovelocity curve displaying a kink from its unperturbed shape.

First, we introduce a quantitative measure for the kink amplitude. Let I_1 be the set of points in an isovelocity curve of a disc hosting a planet and I_0 the corresponding isovelocity curve for the unperturbed disc. If we consider a point $\mathbf{P}_1 \in I_1$, its distance from the curve I_0 is given by

$$\min_{\mathbf{P}_0 \in I_0} [d_E(\mathbf{P}_0, \mathbf{P}_1)], \quad (49)$$

where $d_E(\mathbf{P}_0, \mathbf{P}_1) = [(x_{\mathbf{P}_1} - x_{\mathbf{P}_0})^2 + (y_{\mathbf{P}_1} - y_{\mathbf{P}_0})^2]^{1/2}$. Then, we define the kink amplitude \mathcal{A} as the maximum of the quantity (49) over the points $\mathbf{P}_1 \in I_1$:

$$\mathcal{A} = \max_{\mathbf{P}_1 \in I_1} \left[\min_{\mathbf{P}_0 \in I_0} (d_E(\mathbf{P}_0, \mathbf{P}_1)) \right]. \quad (50)$$

This quantity measures the length of a segment that connects I_1 and I_0 , hence \mathcal{A} has the dimension of a length (Figure 9 shows the geometrical interpretation of (50)). With this tool we studied the dependence of the kink amplitude on the planet mass and on the channel velocity of the isovelocity curve.

We adopted the system parameters of the source HD 163296 studied in Pinte et al. (2018). We considered the channel velocities $v_{\text{ch}}/(\text{km/s}) \in \mathcal{V} = \{1.2, 1.35, 1.5, 1.65, 1.8\}$, chosen such that

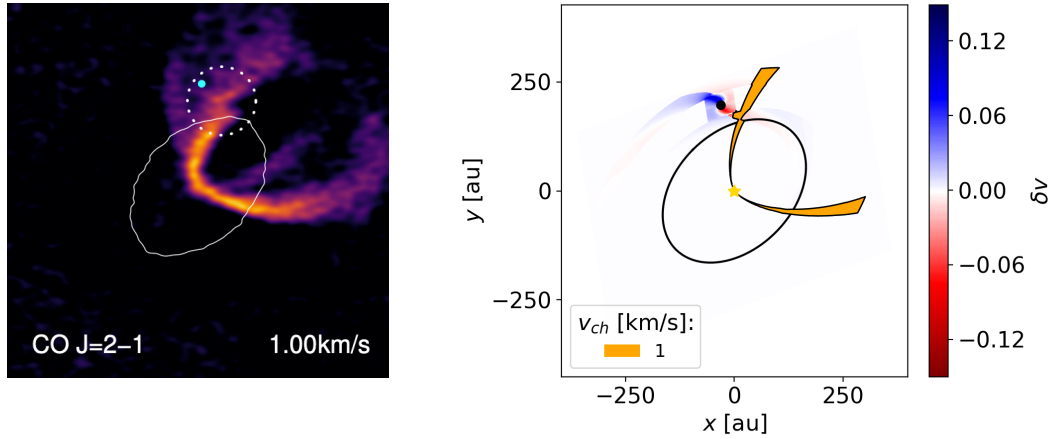


Figure 8. The left panel (Credit: [Pinte et al. 2018](#)) shows the channel map of ^{12}CO line emission at +1 km/s from the systemic velocity of the source HD 163296. The kink in the emission is highlighted by the dotted circle. The potential planet location is marked by a cyan dot. In the right panel the corresponding theoretical channel map is shown. The contour of δv appears in blue and red. In both images the ellipses represents the edge of the dust disc.

the corresponding channel maps, shown in Fig. 10, cross the inner wake (the branch inside the planet orbital radius). For each channel velocity in \mathcal{V} we computed the kink amplitude \mathcal{A} of the kink nearer to the planet, for different planet masses $M_p/M_{\text{Jupiter}} \in \{0.5, 1, 1.5, 2, 2.5, 3, 3.5, 4\}$.

Figure 11 shows the results. We observe that for a fixed planet mass, the kink amplitude grows as channels move closer to the planet (see Figure 10). This is expected since near the planet the interaction with the disc is stronger and then the kinks arising from the resulting velocity perturbations are likely to be more prominent. In other words, the kink amplitude becomes larger as $v_{\text{ch}} \rightarrow v_{\text{ch,p}}$, where $v_{\text{ch,p}} = v_{\text{K}}(r_p) \sin \theta \sin \varphi_p$ is the channel velocity corresponding to the line of sight projection of the planet Keplerian motion. For the system parameters shown in Figs. 10 and 11, $v_{\text{ch,p}} \approx 0.68$ km/s.

Moreover, for a fixed channel velocity, the curves in Figure 11 show that the kink amplitude increases with planet mass. Indeed, a more massive planet generates a stronger velocity perturbation and hence a greater Δv_n (Eq. 40) which implies a larger deviation of the isovelocity curve from its unperturbed shape. In addition, the proportionality between \mathcal{A} and M_p weakens as we move away from the planet (curves from top to bottom), approaching a $\mathcal{A} \propto M_p^{1/2}$ dependence (at least for the lowest considered masses). This behavior is in agreement with the velocity perturbations dependence on the planet mass, which is linear near the planet, becoming less steep in the nonlinear regime where the height of the N-wave lobes asymptotically approach a $\propto M_p^{1/2}$ scaling. We found similar results for the dependence of \mathcal{A} on v_{ch} and M_p when considering channel maps crossing the outer wake.

Finally, there is another geometrical factor that affects the kink amplitude, related to the position of the kink with respect to the major-axis of the disc. Namely, the kink amplitude depends on the quantity Δv_n . Let us consider the simple case where the disc major axis is the y -axis. From Eq. (40) we see that when the planet lies on the x -axis ($\varphi_p = 0$ or $\varphi_p = \pi$) the amplitude of a kink in its neighbourhood will be related to $\Delta v_n \approx \mp u \sin \theta$. On the other hand, when the planet is on the y -axis ($\varphi_p = \pm\pi/2$) we have $\Delta v_n \approx \pm v \sin \theta$. In addition, from Equations (26) and (27) it follows that the azimuthal velocity perturbation v is smaller than u by a factor h_p/r_p . Therefore Δv_n will be larger when the planet is situated near the minor axis, as can be seen in Figure 6, where Δv_n appears to be smaller near the

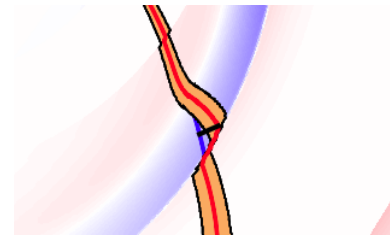


Figure 9. The channel map in orange shows a kink as it crosses the wake. The center of the channel map (red line) is displaced from its unperturbed position (blue line). The length of the black segment linking the two lines is the measure (50) of the kink amplitude.

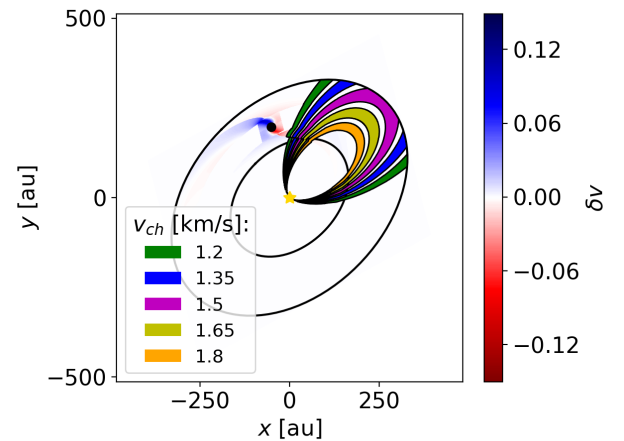


Figure 10. The channel maps of the system HD 163296 considered to study the kink amplitude dependence on the planet mass and channel velocity. The inner ellipses represents the dust disc edge whereas the outer ellipses marks the edge of the gaseous disc.

y -axis. As a consequence, also the kink amplitude will be larger near the minor-axis. Confirmation of this feature can be found in [Pérez et al. \(2018\)](#), where hydrodynamic simulations of protoplanetary discs revealed that the “wiggles” in the first moment maps caused

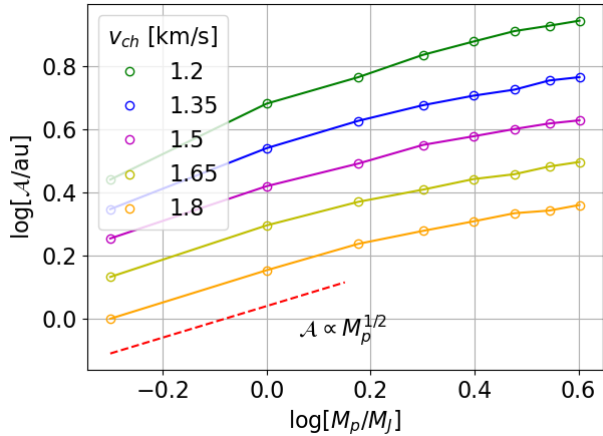


Figure 11. Kink amplitude dependence on the planet mass for the channel maps of Fig. 10.

by the planet-induced velocity perturbations were more pronounced when the planet was located near the disc minor-axis.

4 DISCUSSION

In this paper we have developed a semi-analytic theory for the ‘kink’ perturbation induced in channel maps of line emission by a planet embedded in a circumstellar disc. The basic procedure for predicting the velocity perturbation caused by the planet is as follows:

- (i) Solve for the linear structure of the wake in the vicinity of the planet in the shearing-sheet approximation using a Fast Fourier Transform, similar to the procedure in GR01
- (ii) Use this as the boundary condition for computing the non-linear structure of the wake by solving the corresponding Burger’s equation (10) numerically, as in R02.
- (iii) Relate the radial and azimuthal velocity perturbation amplitudes to the density perturbation via (26) and (27), multiplying these by an optional damping term (46).
- (iv) Add the perturbations to the unperturbed Keplerian velocity profile (38) and project at the desired position angle and inclination to find the line of sight velocity component (39).
- (v) Compute synthetic channel maps, comparing the amplitude of the kink defined via (50) to that measured from the observations.

There are three main limitations to our analytic model. First, the theory of GR01 and R02 is only technically valid for non-gap-opening planets with mass below the thermal mass (8), which is $\approx 0.7 M_{\text{Jup}}$ for a disc with an aspect ratio $h_p/r_p = 0.1$ around a solar mass star. This may be problematic given inferred planet masses of 2–3 M_{Jup} for the kinks observed by Pinte et al. (2018, 2019). Planet masses above the thermal mass cause a deviation from GR01 and R02 theory because the linear and non-linear evolution of the waves can no longer be separated, as the waves launch already in a non-linear fashion. Furthermore, planets above the thermal mass should open a gap, which changes the assumed background surface density. Mitigating this is that the kink is due to the non-linear part of the wake located outside the planet gap, where the azimuthally-averaged disc surface density is relatively undisturbed. Indeed the comparison with the observations in Figure 8 suggests that these effects are not too severe. However, a more detailed comparison of our analytic

predictions with 3D hydrodynamical simulations would be useful to quantify this, similar to the comparison with R02 already performed in Zhu et al. (2015). A possible improvement would be to use a prescribed gap profile for the background surface density (e.g. Crida et al. 2006), but this would still leave the problem of overlapping linear/non-linear regimes.

Second, the analytic theory has only been developed in two dimensions, meaning that it assumes no vertical motion. While the vertical motions induced by the planet are smaller than the radial and azimuthal velocity perturbations (see e.g. supplementary material in Pinte et al. 2019), they are not negligible. We have also assumed a thin disc with a sound speed that is prescribed as a function only of radius, which excludes the possibility of vertical temperature stratification — causing refraction of the waves producing the planet wake — and buoyancy, which can induce additional vertical motion (Bae et al. 2021). Also, the CO emitting layer that is commonly used to detect planetary kinks is located at $\approx 3 - 4$ pressure scale-heights from the midplane, thus inducing projection effects that are not taken into account in 2D, as mentioned in section 3.2.

Third, the analytic theory also assumes a single embedded planet on a circular orbit in the plane. Hence the kink signature may be different for a planet on an inclined or eccentric orbit. This limits the application to a subclass of observed discs. For example, there are at least two planets imaged in the PDS 70 disc (Keppler et al. 2019; Haffert et al. 2019) which models suggest are on eccentric orbits (Bae et al. 2019; Muley et al. 2019; Toci et al. 2020).

Finally, we have also not considered the effects of noise, radiative transfer, chemistry or other real-world complications in producing our synthetic line emission maps.

In step iv) of the above we have assumed that the kink seen in the channel maps is entirely caused by the planet wake. That this succeeds in reproducing the observed kink morphology suggests that this hypothesis is indeed correct and that the kink is caused by the planet wake and not by a circumplanetary disc (Perez et al. 2015) or radial inflow into a gap (Teague et al. 2018). The caveat is that — in contrast with observations and the results of 3D hydrodynamical simulations (Pinte et al. 2018, 2019) — we found that additional, albeit weaker, kinks should be visible further away from the planet, each time the channel maps cross the wake (Figure 6). One possible reason for this in the analytic theory is the absence of additional damping caused by viscosity or other small scale motion. We hence extended this theory to include the effect of additional damping as would be caused by a Shakura-Sunyaev α -viscosity. Adding such damping produced results more in agreement with previous findings, where we require $am \approx 0.5$, where m is the order of the Lindblad resonance dominating the wake. The strongest angular momentum exchange between the planet and disc occurs at the Lindblad resonances with $m \sim r_p/h_p = 10$ (Rafikov 2002), suggesting $m \sim 10$ but this would imply excess viscosity compared to the 3D simulations and compared to observational constraints on small scale motions in protostellar discs by Flaherty et al. (2018, 2020). Note that Dong et al. (2011) showed numerically that viscous damping of nonlinear waves excited by sub-thermal planet masses can be significant even at low viscosity $\alpha \sim 10^{-4}$, which may indicate that the damping prescription adopted by us (Eq. 47) underestimates the actual non-linear damping, reducing the need for high viscosity. Another possibility for the lack of the additional kinks further away from the planet is that wake damping is caused by thermodynamic effects, as discussed by Miranda & Rafikov (2020). A final possibility is that the secondary kinks might simply be washed out by observational effects, including a finite beam size and spectral resolution, and that CO emission is

not produced in the midplane. We intend to explore further all the issues above in subsequent papers in this series.

While we have demonstrated that the analytic theory for planet-disc interaction indeed produces kinks with roughly the correct morphology compared to the observations, our aim in subsequent papers in this series will be to develop this into a parameterised and automated fitting technique for measuring the planet mass with error bars. Further worthwhile effort could be spent in extending the theory to three dimensions, to multiple planets on eccentric or inclined orbits, and perhaps also to considering not only the gas but also the dust component (e.g. [Dipierro et al. 2018](#)).

5 CONCLUSIONS

Disc kinematics offers a new, potentially very powerful technique to detect newly born planets that are still embedded in their natal disc. Such perturbations result in peculiar “kinks” in the channel maps of different gas species, such as CO, when observed at high spatial and spectral resolution with the Atacama Large Millimetre Array (ALMA). A limitation of this method has been the absence of a general theory relating the observed perturbations to the planet properties, meaning that the observed channel maps are usually compared to computationally expensive hydrodynamical simulations, preventing a proper fitting for the relevant system parameters. Here, we have provided such an analytic theory, by extending previous analyses of the disc response to the presence of a massive planet both in the linear and in the non-linear regime. We:

- (i) confirm that the observed kinks are consistent with the planet-induced wake;
- (ii) provide quantitative relations between the kink amplitude and planet properties;
- (iii) showed how to extend the theory to include the effects of damping, such as that caused by disc viscosity, which may be needed in order to have localized kinks that appear only in a limited range of velocity channels.

Our semi-analytic model is intended to form the basis of a more quantitative analysis of the gas kinematics in planet-hosting discs.

ACKNOWLEDGEMENTS

We thank the referee, Ruobing Dong, for useful comments that helped us to improve the presentation. DJP and CP acknowledge funding from the Australian Research Council via FT130100034, DP180104235 and FT170100040. We received funding from the European Union’s Horizon 2020 research and innovation program under the Marie Skłodowska-Curie grant agreement NO 823823 (RISE DUSTBUSTERS project). We thank Roman Rafikov, Cathie Clarke, Giovanni Rosotti and Valentin Christiaens for interesting discussions.

DATA AVAILABILITY STATEMENT

The code used to compute velocity perturbations and produce figures is publicly available at https://github.com/fbollati/Analytical_Kinks.

REFERENCES

- ALMA Partnership et al., 2015, *ApJ*, 808, L3
 Andrews S. M., et al., 2018, *ApJ*, 869, L41
 Ansdell M., et al., 2018, *ApJ*, 859, 21
 Artymowicz P., Penny A., Lagrange A., Russell S., 2000, in ASP Conference Series. p. 13
 Bae J., et al., 2019, *ApJ*, 884, L41
 Bae J., Teague R., Zhu Z., 2021, arXiv e-prints, p. [arXiv:2102.03899](https://arxiv.org/abs/2102.03899)
 Casassus S., Pérez S., 2019, *ApJ*, 883, L41
 Crida A., Morbidelli A., Masset F., 2006, *Icarus*, 181, 587
 Dipierro G., Price D., Laibe G., Hirsh K., Cerioli A., Lodato G., 2015, *MNRAS*, 453, L73
 Dipierro G., et al., 2018, *MNRAS*, 475, 5296
 Dong R., Rafikov R. R., Stone J. M., 2011, *ApJ*, 741, 57
 Dong R., Liu S.-Y., Fung J., 2019, *ApJ*, 870, 72
 Facchini S., et al., 2019, *A&A*, 626, L2
 Flaherty K. M., Hughes A. M., Rosenfeld K. A., Andrews S. M., Chiang E., Simon J. B., Kerzner S., Wilner D. J., 2015, *ApJ*, 813, 99
 Flaherty K. M., Hughes A. M., Teague R., Simon J. B., Andrews S. M., Wilner D. J., 2018, *ApJ*, 856, 117
 Flaherty K., et al., 2020, *ApJ*, 895, 109
 Fung J., Chiang E., 2016, *ApJ*, 832, 105
 Goldreich P., Tremaine S., 1979, *ApJ*, 233, 857
 Goldreich P., Tremaine S., 1980, *ApJ*, 241, 425
 Goodman J., Rafikov R. R., 2001, *ApJ*, 552, 793
 Haffert S. Y., Bohn A. J., de Boer J., Snellen I. A. G., Brinchmann J., Girard J. H., Keller C. U., Bacon R., 2019, *Nature Astronomy*, 3, 749
 Horne K., Marsh T. R., 1986, *MNRAS*, 218, 761
 Huang J., et al., 2018, *ApJ*, 869, L43
 Keppler M., et al., 2018, *A&A*, 617, A44
 Keppler M., et al., 2019, *A&A*, 625, A118
 Kraus S., et al., 2020, arXiv e-prints, p. [arXiv:2004.01204](https://arxiv.org/abs/2004.01204)
 Lin C. C., Shu F. H., 1964, *ApJ*, 140, 646
 Lodato G., et al., 2019, *MNRAS*, 486, 453
 Long F., et al., 2018, *ApJ*, 869, 17
 Miranda R., Rafikov R. R., 2020, *ApJ*, 892, 65
 Muley D., Fung J., van der Marel N., 2019, *ApJ*, 879, L2
 Ogilvie G. I., Lubow S. H., 2002, *Monthly Notices of the Royal Astronomical Society*, 330, 950
 Papaloizou J., Lin D. N. C., 1984, *ApJ*, 285, 818
 Perez S., Dunhill A., Casassus S., Roman P., Szulágyi J., Flores C., Marino S., Montesinos M., 2015, *ApJ*, 811, L5
 Pérez L. M., et al., 2016, *Science*, 353, 1519
 Pérez S., Casassus S., Benítez-Llambay P., 2018, *MNRAS*, 480, L12
 Pinte C., et al., 2018, *ApJ*, 860, L13
 Pinte C., et al., 2019, *Nature Astronomy*, 3, 1109
 Pinte C., et al., 2020, *ApJ*, 890, L9
 Rafikov R. R., 2002, *ApJ*, 569, 997
 Shakura N. I., Sunyaev R. A., 1973, *A&A*, 500, 33
 Shu F. H., 1984, in Greenberg R., Brahic A., eds, IAU Colloq. 75: Planetary Rings. pp 513–561
 Teague R., Bae J., Bergin E. A., Birnstiel T., Foreman-Mackey D., 2018, *ApJ*, 860, L12
 Teague R., Bae J., Bergin E. A., 2019, *Nature*, 574, 378
 Toci C., Lodato G., Christiaens V., Fedele D., Pinte C., Price D. J., Testi L., 2020, *MNRAS*, 499, 2015
 Trapman L., Facchini S., Hogerheijde M. R., van Dishoeck E. F., Bruderer S., 2019, *A&A*, 629, A79
 Veronesi B., et al., 2020, *MNRAS*, 495, 1913
 Whitham G., 1974, *Linear and Nonlinear Waves*. Wiley, <https://books.google.it/books?id=f8oRAQAIAAJ>
 Zhang S., et al., 2018, *ApJ*, 869, L47
 Zhu Z., Dong R., Stone J. M., Rafikov R. R., 2015, *ApJ*, 813, 88
 van der Marel N., et al., 2013, *Science*, 340, 1199

This paper has been typeset from a $\text{\TeX}/\text{\LaTeX}$ file prepared by the author.